Biomimetic flow control

Superhydrophobic surfaces: From the lotus leaf to the submarine

Mohamed A. Samaha, Hooman Vahedi Tafreshi, Mohamed Gad-el-Hak *

Department of Mechanical & Nuclear Engineering, Virginia Commonwealth University, Richmond, VA 23284-3015, USA

A B S T R A C T

In this review we discuss the current state of the art in evaluating the fabrication and performance of biomimetic superhydrophobic materials and their applications in engineering sciences. Superhydrophobicity, often referred to as the *lotus effect*, could be utilized to design surfaces with minimal skin-friction drag for applications such as self-cleaning and energy conservation. We start by discussing the concept of the *lotus effect* and continue to present a review of the recent advances in manufacturing superhydrophobic surfaces with ordered and disordered microstructures. We then present a discussion on the resistance of the air–water interface to elevated pressures—the phenomenon that enables a water strider to walk on water. We conclude the article by presenting a brief overview of the latest advancements in studying the longevity of submerged superhydrophobic surfaces for underwater applications.

© 2011 Académie des sciences. Published by Elsevier Masson SAS. All rights reserved.

1. Introduction

Several design ideas have been inspired by nature. Biological mechanisms can be studied to engineer systems for modern industrial applications. The lotus leaf possesses a peculiar water-repellent characteristic that enhances the mobility of droplets for self-cleaning purposes [1]. A similar effect, i.e. superhydrophobicity, enables a water strider to walk on water [2]. When a superhydrophobic surface is fully submersed in water, it entraps air in its pores resulting in the formation of air pockets between the solid surface and water. The entrapped air is separated from water with a thin interface anchored on the solid walls and stretched due to surface tension forces. It has been observed that a moving body of water "slips" over an air–water interface, whereas it "sticks" to a solid surface [3]. Therefore, if the percentage of the surface covered by air pockets is sufficiently high, a superhydrophobic surface can cause the so-called "slip effect", resulting in a reduction in the skin-friction drag exerted on the surface [3]. As long as the air pockets exist, the surface remains hydrophobic. In other words, the degree of hydrophobicity and the beneficial effects are diminished by the reduction of the amount of entrapped air. The longevity of a superhydrophobic surface—how long the surface can maintain the air pockets—is critical, especially in underwater applications.

Engineered superhydrophobic surfaces are often comprised of microridges or microposts arranged in an ordered configuration on a solid flat surface. These surfaces have been extensively studied and developed to produce slip effect [4]. Large-scale manufacturing of such surfaces, however, is prohibitively expensive. On the contrary, surfaces manufactured by random deposition of hydrophobic particles [5–7] or fibers [8–11] could offer more cost-effective alternatives for production of large superhydrophobic surfaces, as will be discussed later in this article.

In the next section, we discuss the lotus leaf effect and the underlying fluid mechanics of slip effect. In Section 3, we review the different manufacturing techniques used for fabrication of superhydrophobic surfaces. In Section 4, we discuss

---

* Corresponding author.
  E-mail addresses: samahama@vcu.edu (M.A. Samaha), htafreshi@vcu.edu (H.V. Tafreshi), gadelhak@vcu.edu (M. Gad-el-Hak).
  URLs: http://www.people.vcu.edu/~htafreshi/ (H.V. Tafreshi), http://www.people.vcu.edu/~gadelhak/ (M. Gad-el-Hak).
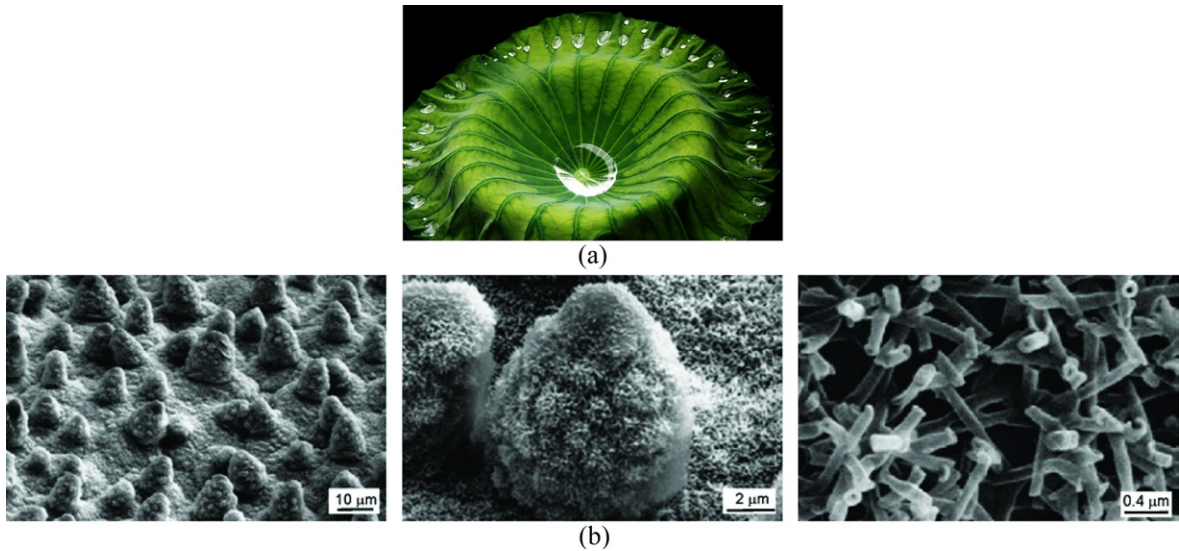
Fig. 1. Lotus leaf: (a) Magnification of one. From website [14]; (b) Three different magnification of SEM images showing morphological micro- and nanostructures. From Koch et al. [13].
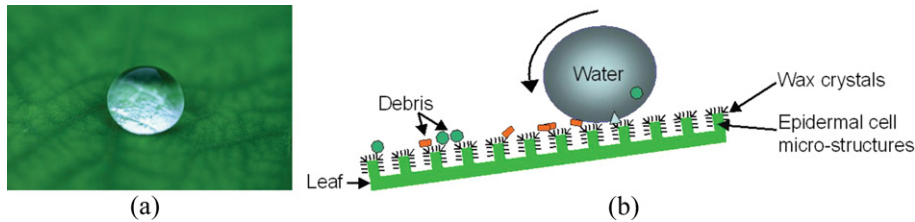

Fig. 2. (a) Water droplet beading on lotus leaf with static contact angle higher than 150 degrees. From website [15]; (b) Schematic illustration of lotus effect. From website [16].

the stability of the air–water interface under elevated pressures, the key concept that allows water to support the weight of a water strider. In Section 5, we present a discussion on the latest advances in measuring the longevity of submerged superhydrophobic surfaces. In the "Future outlook" section, we give suggestions and recommendations to improve and enhance the current fabricated surfaces. This will be followed by our conclusions, given in Section 7.

2. Characterization of superhydrophobic surfaces: the lotus effect

2.1. Lotus leaf

Lotus leaves, *Nelumbo nucifera*, owe their self-cleaning ability to superhydrophobicity. Neinhuis and Barthlott [1] obtained scanning electron microscopy (SEM) images for several water-repellent plants and reported the micromorphological characteristics of 200 species. They demonstrated that the epidermal (i.e. outermost) cells of the lotus leaves form papillae, which act as microstructure roughness. The papillae are superimposed by a very dense layer of epicuticular waxes (wax crystals), also referred to as hair-like structures [12] or nanostructure roughness [13]. Fig. 1 shows different degrees of magnification of lotus leaves using SEM images from one to 10^6 times. Epicuticular waxes themselves have hydrophobic properties, which together with micro- and nanostructure roughness, result in reduced contact area between water droplets and the leaf's surface. This combination results in static contact angles exceeding 150 degrees on lotus leaves. If the surface is tilted, even with a slight angle, water droplets begin to roll off the leaves, and so collect and remove dirt from the surface demonstrating the self-cleaning effect (see Fig. 2). Note that because of the micro- and nanostructure roughness, the contact area between dirt particles and the leaf's surface is dramatically reduced. Thus, the adhesion between the particles and the surface can be lower than that between the particles and the droplets, facilitating particle removal. Accordingly, the lotus leaf is a symbol of purity in some Asian religions [1].

To demonstrate the importance of nanoscale wax crystals on the lotus effect, Cheng et al. [12] altered the surface structure of a lotus leaf without affecting the chemical composition. They heated the leaf to 150 °C (thermal annealing) to melt the waxy crystals, leaving the microstructures intact, and found a decrease in the static contact angle of the treated leaf. Neinhuis and Barthlott [1] reported that the lotus effect tends to keep the leaves dry, which helps to protect the plant against pathogens such as fungi by denying these parasitic organisms the moisture that they require to germinate. Moreover,
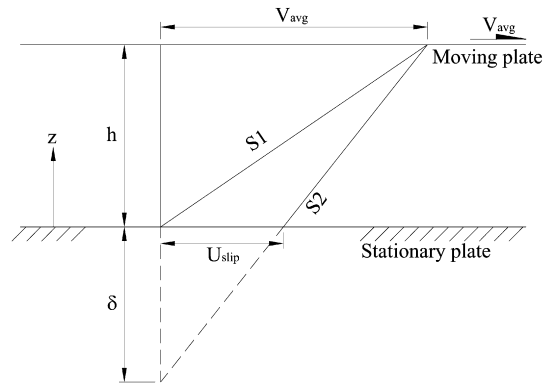
Fig. 3. Schematic diagram of velocity profiles between fixed and moving plates in case of slip and no slip at fluid–solid interface. From Samaha et al. [18].

since CO_2 diffuses 10^4 times faster in air than in water, the water-repellent leaves allow CO_2 to be more easily absorbed, ensuring an adequate supply of CO_2 for photosynthesis, even in habitats with high air humidity [1].

2.2. Slip flow and drag reduction

When a superhydrophobic surface is submersed in water, it generates slip flow, which reduces the skin-friction drag exerted on the surface. Drag is the force produced by a fluid to resist the relative motion of a solid [17]. A tremendous amount of fuel is consumed each year both by air and water vehicles and by gas and liquid transmission through pipelines in order to overcome drag [17]. Drag force can be classified into two main categories, form (pressure) drag and skin-friction drag. The latter, which depends on fluid viscosity, strain rate (velocity gradient), and surface area, is the subject of this section. The multiplication of fluid viscosity and velocity gradient gives the shear stress. Fig. 3 shows the Couette flow between two plates having a gap, h, in the normal direction, z. The upper plate is moving with velocity V_{avg} and the lower one is stationary. The lower plate can have a no-slip (sticky) or a slip boundary condition. In the case of no-slip boundary, the slope of the velocity gradient (line S1) is higher than that of slip flow (line S2), which leads to a higher shear stress.

Generally, slip is defined as a fluid dynamics condition in which there exists a relative tangential velocity between the solid surface and the fluid immediately adjacent to the surface. Slip can be encountered in several situations. For example, for gas flow, slip could occur if the mean free path of the gas (i.e. the average distance traveled by molecules between collisions) is comparable to the characteristic dimensions of the flow [19]. As mentioned earlier, a superhydrophobic surface entraps air in its pore space producing two different interfaces. One is the aforementioned air–water interface on which the water slips, and the other is the solid–water interface to which the water sticks. The average slip over the entire surface is often referred to as "effective slip" [20]. The air–water interface area is characterized by the gas fraction, the ratio of the area of the air–water interface to the total surface area. The gas fraction is the main parameter that determines the static contact angle [21], which characterizes the hydrophobicity of the surface. Callies et al. [22] experimentally demonstrated that as gas fraction increases, static contact angle increases. Furthermore, the gas fraction has an impact on the so-called "slip length, δ" [23]. According to Navier's model [24], the magnitude of the slip velocity is proportional to the magnitude of the strain rate. The slip length is the proportionality constant as shown in Fig. 3. Thus, the slip length can be calculated from the following equation:

$$\delta = \frac{U_{slip}}{\frac{\partial u}{\partial y}\big|_{wall}} \tag{1}$$

where U_{slip} is the area-weighted average slip velocity at the superhydrophobic wall, u is the streamwise velocity, and y is the normal direction.

Several studies have demonstrated the effect of the gas fraction on the slip length [23,25–36]. Some of these studies showed that for laminar flow, slip length increases as gas fraction increases (Fig. 4) and hence from Eq. (1), velocity gradient decreases (i.e. less drag). This figure shows the calculated and the measured slip lengths (normalized by the pitch; the distance between two posts) versus gas fraction for ordered microposts on a superhydrophobic surface. A closer view at gas fractions below 0.6 and above 0.85 is given in the insets for better illustration. From the figure, it is obvious that when the gas fraction, ϕ_g, is less than 0.4, the slip length is proportional to ϕ_g^2. On the other hand, if the gas fraction is higher than 0.7, the slip length is proportional to $1/\sqrt{\phi_g}$. Within the range $0.4 < \phi_g < 0.7$, interpolation is utilized. The above mathematical proportionalities are derived and validated by Ybert et al. [30]. The drag reduction also increases as gas fraction increases, as shown in Fig. 5. The figure includes both experimental and numerical results for a microchannel with a microridged superhydrophobic wall.
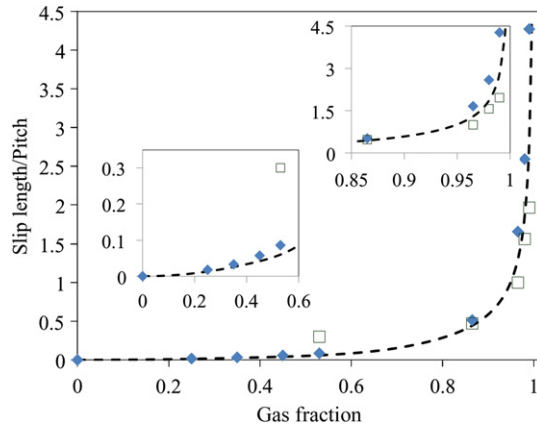
Fig. 4. Slip length vs. gas fraction obtained for laminar flow over ordered microposts superhydrophobic surface. Experimental data of Lee et al. [23] (open squares), theory of Ybert et al. [30] (dashed line), and Samaha et al. [36] (solid diamonds).
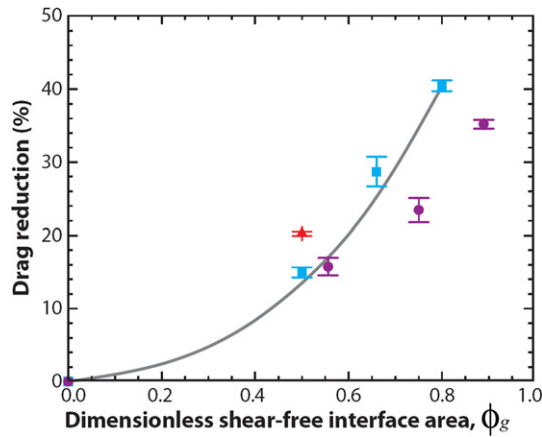

Fig. 5. Average drag reduction as a function of dimensionless shear-free area, gas fraction. 30 μm wide microridges spaced 30 μm apart (triangles), 20 μm wide microridges spaced 20 μm apart (squares), and 30 μm square microposts spaced 30 μm apart (circles). Numerical results for 20 μm wide microridges spaced 20 μm apart (gray line). From Rothstein [3].
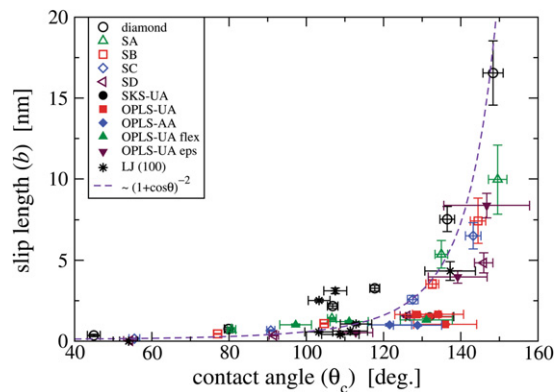

Fig. 6. Slip length of water as a function of contact angle on various smooth surfaces. The results are obtained by Huang et al. [37] using molecular dynamics simulations.

The slip boundary condition has been studied theoretically using molecular dynamics (MD) simulations [37–39]. These simulations convincingly demonstrated that the greater the hydrophobicity of the surface, the larger the slip length will be. Fig. 6 shows computed slip length using MD simulations versus contact angle θ_c for different surfaces [37,38]. The numerical results are curve-fitted using the relation $b \propto (1 + \cos\theta_c)^{-2}$, where b is the slip length. Static contact angles clearly are a measure of the degree of hydrophobicity of a solid surface.
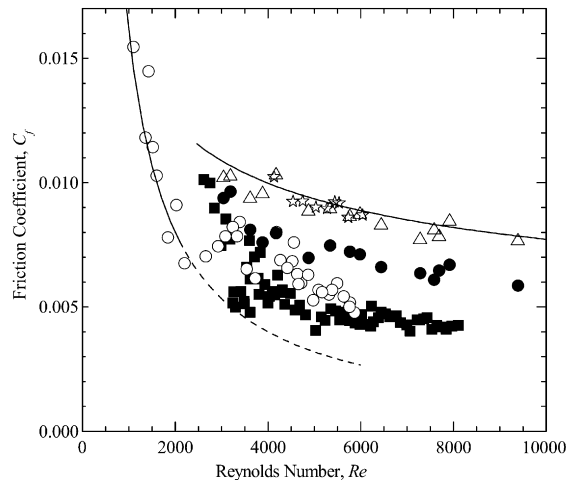
Fig. 7. Skin-friction coefficient vs. Reynolds number. Microchannel with smooth surfaces (open triangles and open stars), with single superhydrophobic wall (solid circles), and with two superhydrophobic walls (open circles and solid squares). The theoretical predictions of the friction coefficient for a smooth channel are also shown (−). From Daniello et al. [32].

Other studies show that for turbulent flows, increasing the shear-free area (i.e. increasing the gas fraction) results in an increase in the slip velocity and drag reduction [32,33]. Fig. 7 shows that skin-friction coefficient decreases by utilizing a superhydrophobic surface on one or both walls of a microchannel for a range of Reynolds numbers covering both the laminar- and turbulent-flow regimes. On the contrary, this was not observed in the work of Woolford et al. [35], who demonstrated that in a turbulent-flow regime, streamwise ridges (i.e. flow direction is parallel to microridges structure) can cause drag reduction, while spanwise ridges (i.e. flow direction is perpendicular to microridges structure) can increase the drag.

Obviously, the influence of the microstructural parameters of a superhydrophobic surface on its performance requires further exploration. Such surfaces could be utilized as a passive method of flow control and may potentially become a viable alternative to the more complex and energy consuming active or reactive methods of flow control such as wall suction/blowing [17].

3. Microfabrication of superhydrophobic surfaces

3.1. Ordered microstructures

Most engineered superhydrophobic surfaces are made up of microposts or microridges (Fig. 8). The microstructure of these surfaces strongly affects the gas fraction, slip length, and drag reduction, in addition to the stability of the air–water interface. For instance, in Fig. 8(a), as post diameter decreases for the same pitch (i.e. distance between two posts), the gas fraction increases, which leads to an increase in the drag reduction and slip length due to the increase of the free shear area (air–water interface area). However, increasing the gas fraction can jeopardize the stability of the interface. Criteria describing the stability based on roughness design were given by Bico et al. [40]. A similar conclusion could be drawn for microridges.

Superhydrophobic surfaces comprised of "nanograss" and "nanobricks" are reported by Henoch et al. [41] (see Fig. 9). The surface with nanograss is reported to yield a contact angle of nearly 180°, and is composed of posts with a diameter of 400 nm and a height of 7 μm spaced 1.25 μm from one another. The surface with nanobricks is peculiar because it can better resist the elevated hydrostatic pressures due to the effect of the entrapped air in its closed cells, which can help to increase the stability of the air–water interface, as will be discussed later in this paper. The size of each cell is 4 μm × 10 μm, the height of the cell walls is about 1 μm, and the thickness of the walls is 300 nm. A surface with a texture somewhat similar to that of the nanograss structure is studied by Choi and Kim [42]. These authors present slip length of their surface in comparison to that of a smooth one. Lee and Kim [4] demonstrated that the slip length can be maximized by superimposing a nanostructure onto a microfabricated structure, similar to the case of wax crystals on papillae of the lotus leaves as shown in Fig. 10. These authors demonstrated that the contact angle for their surfaces can approach 180°. In addition, they showed that the slip length can be increased up to 400 μm.

3.2. Surfaces with engineered roughness

There are limitations for commercializing microfabricated surfaces such as those shown in Figs. 8–10. Production cost is probably the most prohibitive issue with microfabricated surfaces. Recent studies, however, have shown that there are alternative methods for engineering superhydrophobic surfaces more cost-effectively. As discussed by Emami et al. [5], one
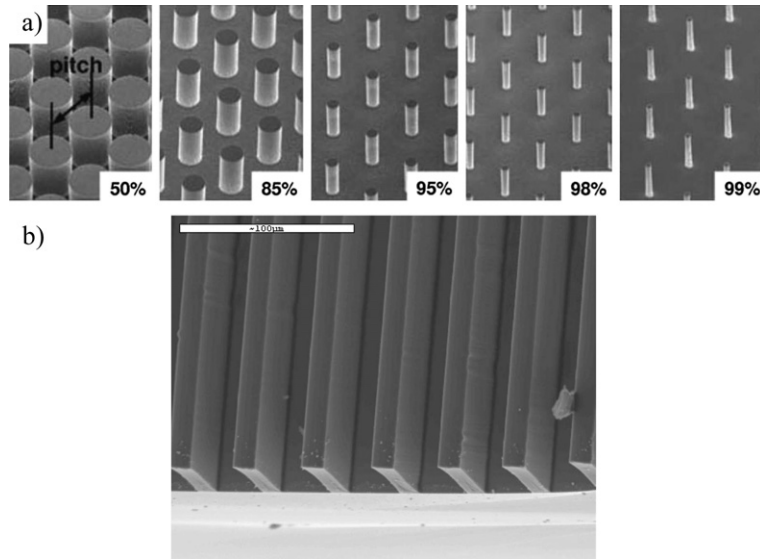
Fig. 8. (a) Scanning electron microscopy (SEM) images of post patterns with 50 μm pitch for the displayed inset gas fractions. From Lee et al. [23]; (b) Image of microfabricated surface with microridges. The width of the cavities and ridges are 30 and 10 μm, respectively. The depth of the rib is 15 μm. From Maynes et al. [29].
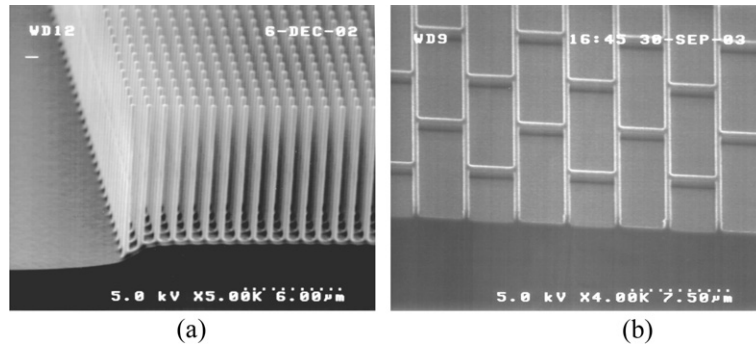

Fig. 9. (a) SEM image of silicon nanograss; (b) SEM image of silicon nanobricks. From Henoch et al. [41].
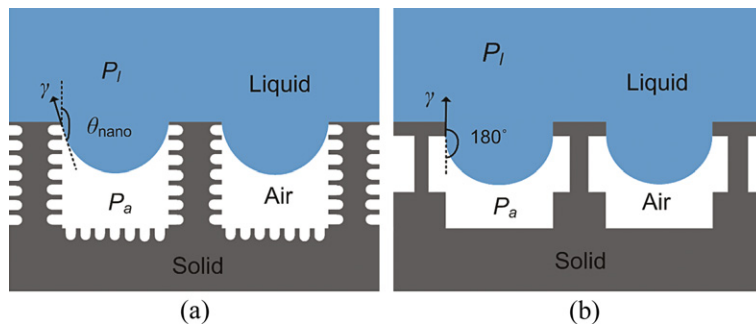

Fig. 10. (a) Nanostructures on the sidewall; (b) Re-entrant structure. From Lee and Kim [4].

can produce a superhydrophobic surface by randomly depositing hydrophobic particles (e.g. aerogel) on a substrate (see also [6,7]). Fig. 11(a) shows an SEM image of aerogel powders synthesized using sodium silicate and deposited on a substrate. The static contact angle is measured for a coated surface with aerogel powders to show its superhydrophobicity. Fig. 11(b) shows that the contact angle for such a surface is 150°.

Samaha et al. [36] simulated the performance of superhydrophobic surfaces having idealized random roughness (posts or particles) and compare their results with those of surfaces manufactured via microfabrication. Their numerical simulations indicated that the gas fraction has a significant impact on the characteristics of a superhydrophobic surface, as it affects the slip length and therefore the skin-friction coefficient. As can be seen in Fig. 12, the friction coefficient decreases with
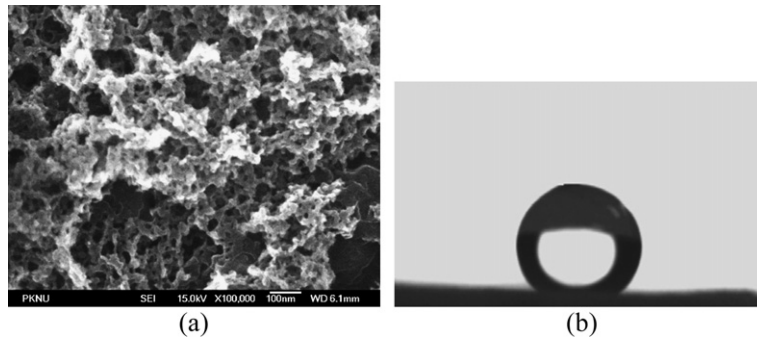
Fig. 11. (a) SEM image of aerogel powders synthesized using sodium silicate; (b) Water droplet placed on surface of glass substrate coated with aerogel powder. The contact angle is 150°. From Bhagat et al. [7].
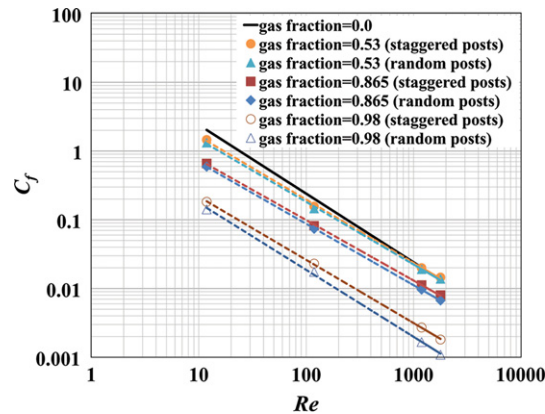

Fig. 12. Skin-friction coefficient versus Reynolds number (Moody diagram) for different gas fractions. From Samaha et al. [36].

increasing gas fraction for surfaces with staggered posts and randomly distributed posts. In addition, the difference between the skin-friction coefficient of the random posts and that of the staggered posts increases by increasing the gas fraction. Thus, the surface with randomly distributed posts possesses better drag reduction than in the case of staggered, distributed posts.

Electrospinning is another cost-effective fabrication technique that can be used to produce superhydrophobic surfaces with fibrous microstructure. This technique can be used to deposit micro- and/or nanotextured coatings by spinning hydrophobic polymers onto substrates of arbitrary geometries [8–11]. Conventionally, electrospinning is performed by applying a large DC-potential between the electrospinning source (typically a hypodermic syringe) and the substrate, resulting in nonwoven fiber mats with randomly oriented fibers [43]. The random orientation of the fibers is the result of the inherent electrostatic instability of the charged jet as it travels from the spinneret to the collector. This instability can be reduced by using a DC-biased AC potential that induces short segments of alternating polarity, thereby reducing the magnitude of the destabilizing force on the fiber (see Fig. 14(a)) [43].

Fig. 14 shows SEM images of fiber mats produced via DC-electrospinning and DC-biased AC-electrospinning. As shown in Fig. 14, DC-biased AC-electrospinning provides a better control over the microstructure of deposited fibrous mats. The insert in Fig. 14(b) shows a water droplet on the coating with a static contact angle of 157 degrees, proving superhydrophobicity even in the case of random fiber deposit [11]. This is because, similar to the case of microfabricated surfaces, such superhydrophobic fibrous coatings can provide the porosity that is necessary to entrap air when the surface is immersed in water. As expected, when water flows over such a surface, a reduction in the skin friction is observed [18].

Samaha et al. [18] measured drag reduction and slip length for such a coating. They used a rheometer made by the Anton Paar Corporation (model Physica MCR 301) equipped with two parallel rotating discs separated by a small fluid-filled gap. One disc is stationary and attached to a water cooling system for temperature control. The second disc rotates at a prescribed speed and is connected to an air bearing to minimize friction. Compressed air at about 6 atm supports the bearing. The rotating disc is connected to a torque–speed measuring system used to calculate the shear stress developed by the fluid, and the measured rotational speed is used to calculate the strain rate. Equations governing this motion are derived to calculate both drag reduction and slip length from the measured stress–strain rate relation. As will be displayed later in this paper, the results of generated drag reduction by the spun-fiber coating are shown in Fig. 28, which confirm the superhydrophobicity of this cost-effective fabricated coating. In addition, the slip length results attained using this fabrication approach are comparable to those obtained using ordered micro/nanostructure surfaces [4].
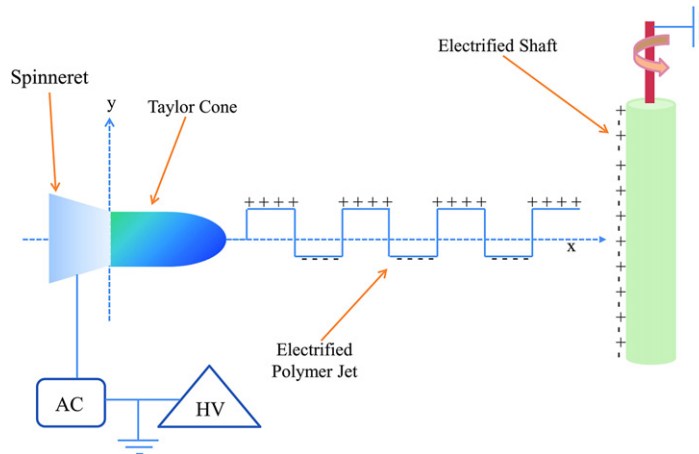
Fig. 13. Schematic illustration of electrified polymer jet during DC-biased AC-electrospinning. From Ochanda et al. [11].
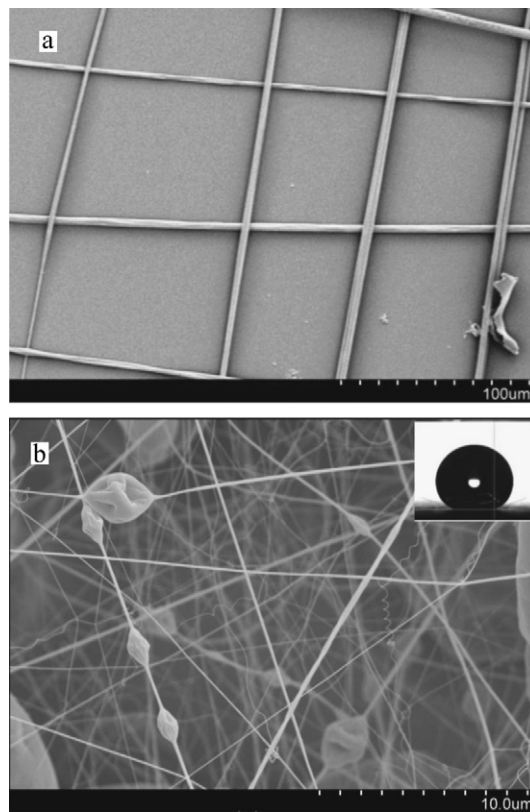

Fig. 14. SEM images of 18% weight polystyrene fibers with 1% weight fluoro-elastomer. (a) Grid-like structure of a mono-layer; (b) Several layers of fibers show random orientation. Upper right insert in (b) shows a water droplet on top of this particular coating. The figure adapted from Samaha et al. [18].

It is worth mentioning that the morphology of the fibers influences the hydrophobicity of the surface. For example, fiber diameter can affect the static contact angle of the coating, as shown in Fig. 15. This figure shows that contact angle decreases with increasing fiber diameter. However, one should note that since other microstructural parameters of the surfaces reported in this figure were not kept constant while fiber diameter was varied, changes in the fiber diameter could have affected the porosity of the mat. Therefore, in the absence of more microstructural information, one should refrain from directly relating fiber diameter to contact angle. The figure shows the results for produced beaded and bead-free fibers. Beaded fibers or polymeric microdroplets could have appeared during electrospinning if the polymeric fluid did not have adequate viscoelasticity and conductivity, which leads to the Rayleigh instability, i.e., domination of surface tension during the process that tends to break the liquid into droplets.
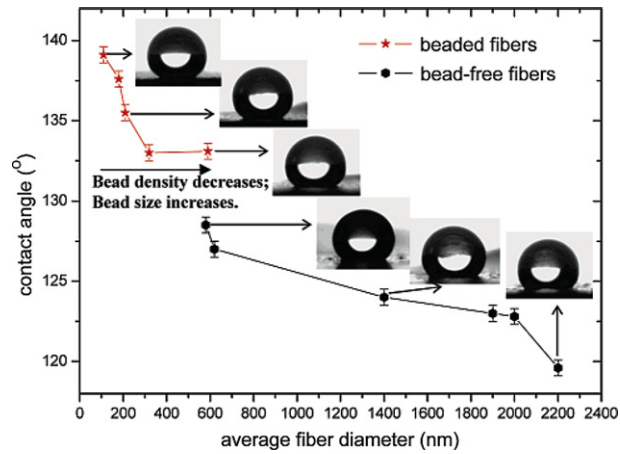
Fig. 15. Effect of fiber's diameter on static contact angle. From Ma et al. [8].
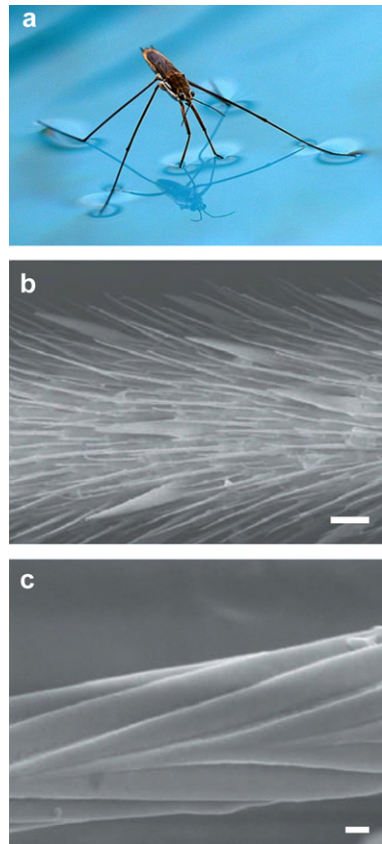

Fig. 16. (a) Water strider stands on water. From website [44]; (b) SEM image of water strider's leg showing hydrophobic microsetae, scale bar 20 μm; (c) Higher magnification of single hair showing nanogrooves, scale bar 0.2 μm. (b) and (c) from Gao and Jiang [2].

4. Stability of air–water interface under elevated pressures: water striders

4.1. Walking on water

Water striders, *Gerris remigis*, possess a very rare trait that allows them to walk on water. Water striders owe this ability to the hydrophobic waxy microhairs covering their legs, microsetae, which are superimposed with nanogrooves [2] as shown in Fig. 16.

Air is entrapped between the micro- and nanostructured hairs, making their legs water repellent. Gao and Jiang [2] used a very sensitive balance system to determine the required force for a single leg to be sunk. They demonstrate that the
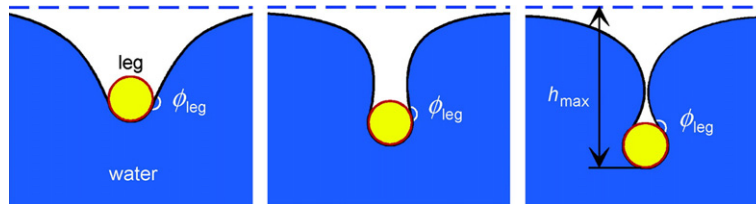
Fig. 17. Transects of the water surface for the leg contacting the water to different depths until the maximum depth h_{max} is reached before piercing the water surface. From Feng et al. [45].
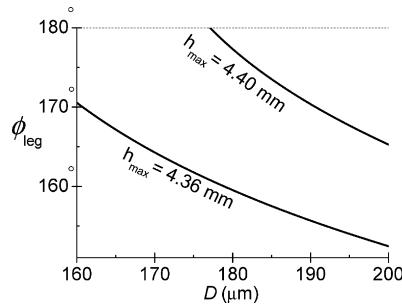

Fig. 18. Contact angle of the leg and dimple depth. Dependence of the contact angle on the diameter of the leg in order to form the maximal dimple with depth $h_{max} = 4.38 \pm 0.02$ mm. From Feng et al. [45].

buoyancy force is 15 times the total body weight. Furthermore, the volume of the displaced water caused by immersing a single leg is 300 times that of the leg itself. Feng et al. [45] have modeled the ultra-hydrophobicity of a water strider's leg by providing a theoretical analysis, coupled with experimental measurements, to determine how deep the leg can reach before piercing the water surface as shown in Fig. 17. They demonstrated that the maximum depth, h_{max}, depends on the diameter, D, and the contact angle of the leg, ϕ_{leg}. Their results are shown in Fig. 18. It can be seen that for the actual diameter range (140–180 μm) and for the measured maximum depth ($h_{max} = 4.38 \pm 0.02$ mm), the contact angle should be at least 168°, i.e. highly water-repellent. Such a high contact angle allows water striders to stand on water, even in the presence of rain or water currents.

Water striders have the ability to flit about quickly, where the propulsive forces on the insect are generated by a combination of form drag and curvature forces [46]. According to Hu et al. [47], water striders use their superhydrophobic legs to create hemispherical vortices, which transfer the momentum beneath the water surface that develops enough hydrodynamic force to propel the insect, similar to using oars to move a boat. Several water-walking machines are inspired by water striders and other insects [48]. The devices are designed and constructed to precisely mimic the natural locomotion mechanisms of the insects.

Water striders are natural predators of spiders and other insects that fall onto the water surface. They use their front legs to sense ripples developed by a falling prey [49] and grab onto it. The superhydrophobicity of a water strider's legs is its survival mechanism, allowing it to float, run on water, and sense prey for feeding. It is worth mentioning that other species such as spiders and several other insects are covered with hydrophobic hairs similar to those of water strider, but for a different purpose. The entrapped air (plastron) is utilized by spiders and similar species for underwater breathing. The mechanics of plastron respiration are demonstrated by Flynn and Bush [50].

4.2. Stability of air–water interface under hydrostatic pressure

The air–water interface developed due to superhydrophobicity is the surface that supports a water strider's weight. A similar force can be exerted on the air–water interface formed over a submerged superhydrophobic surface by the column of water above the surface. If the pressure is high enough, water will penetrate into the pores on the surface and replace the air, i.e. transition from the non-wetted state (Cassie state) to the wetted state (Wenzel state). This transition is interpreted by two approaches: one based on minimizing the thermodynamic free energy [51,52], and the other using a balance of forces across the interface [53–55]. Lee and Kim [4] used the latter to develop an equation to determine the maximum allowable hydrostatic pressure (critical pressure) in terms of the surface microstructure for aligned or staggered arrangement of posts as shown in the following equation:

$$P_{max}\phi_g \leqslant \frac{-2\gamma\sqrt{\pi(1-\phi_g)}\cos\theta}{L} \tag{2}$$
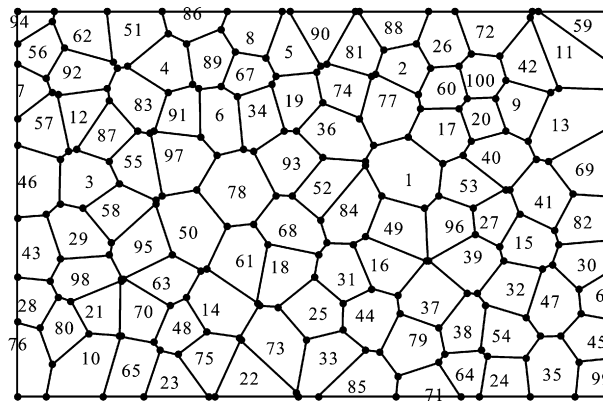
Fig. 19. Voronoi diagram obtained for randomly distributed posts. The numbers shown in this figure refer to the posts and their locations. From Samaha et al. [36].
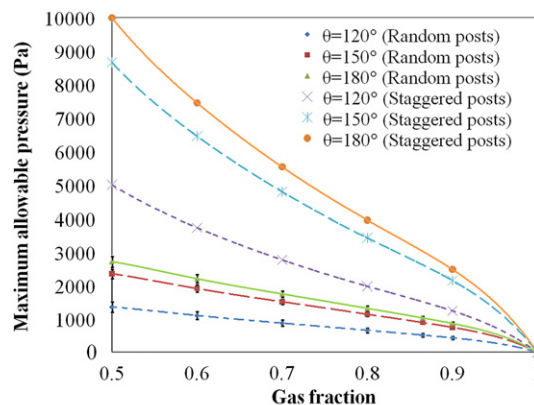

Fig. 20. Maximum allowable pressure as a function of gas fraction and contact angle for both random and staggered posts. From Samaha et al. [36].

where P_{max} is the critical pressure, the pressure above which the system departs from the Cassie state, ϕ_g is the gas fraction, γ is the surface tension of the liquid (72×10^{-3} N/m in case of water), θ is the contact angle, and L is the pitch (distance between two posts).

Samaha et al. [36] utilized a Voronoi diagram [56] to determine the local gas fraction and the maximum pitch for superhydrophobic surfaces made up of randomly distributed posts. This information is used in Eq. (2) to determine the maximum allowable hydrostatic pressure, which corresponds to the post that has the maximum local gas fraction. In a Voronoi diagram, the superhydrophobic surface is divided into cells, as shown in Fig. 19. Each post has a single surrounding Voronoi cell consisting of all points on the surface that are closer to that post than to any other post. The sides of a Voronoi cell are the locations of the points on the surface that are equidistant from the two nearest posts. The Voronoi nodes are the points equidistant from three (or more) posts. Note that a Voronoi diagram provides a *rational* tool to compute the *local* gas fraction and maximum pitch when dealing with random posts.

The maximum allowable pressures for surfaces comprised of random and staggered posts are compared with each other in Fig. 20. It can be seen that the maximum allowable pressure decreases dramatically when the posts are arranged randomly. The results of this figure indicate that superhydrophobic surfaces with random roughness are more susceptible to failure under hydrostatic pressures. Therefore, although random posts can result in a better drag reduction (see Fig. 12), they are more likely to fail under elevated pressures.

Emami et al. [5] conducted a similar study in 3-D space. In particular, they simulated the stability of air–water interface formed on granular superhydrophobic coatings comprised of randomly distributed spherical aerogel particles in comparison to the ordered distributed ones. These authors also conducted a series of 3-D full-morphology (FM) numerical simulations and analytical expressions to predict the critical pressure (pressure beyond which the surface departs from the Cassie state) against solid volume fraction of their granular porous coatings, as shown in Fig. 21. This figure shows that the air–water interface can sustain more pressure as the solid volume fraction increases. Moreover, the surface with random particles is more susceptible to failure under hydrostatic pressure, as expected.

Emami et al. [57] developed a mathematical framework to calculate the exact shape of the air–water interface, and so predict the stability of the air–water interface on superhydrophobic surfaces made up of randomly distributed posts of different diameters, heights, and materials. This was accomplished by using the Young–Laplace equation to derive a second-
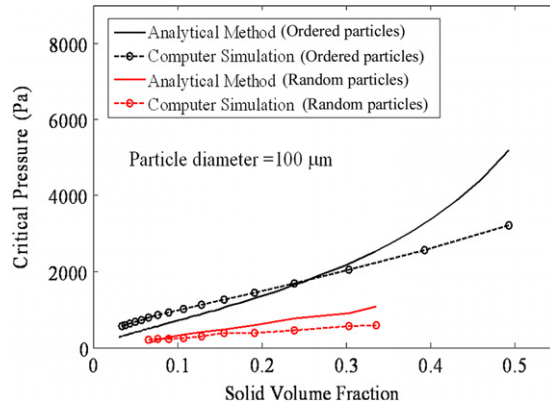
Fig. 21. Numerically and analytically calculated critical pressure against solid volume of fraction for ordered aerogel particles and random ones. Figure adapted from Emami et al. [5].
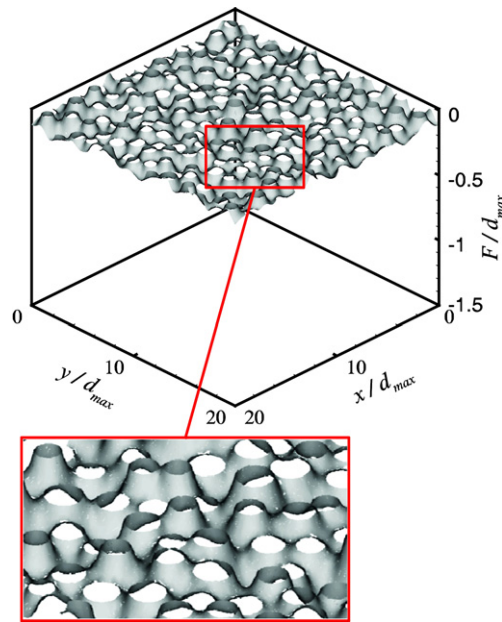

Fig. 22. Calculated meniscus surfaces for superhydrophobic surface with randomly distributed posts of random diameters and heights at $P = 3400$ Pa. d_{max} refers to maximum post's diameter. x, y, and F are Cartesian coordinates. Figure adapted from Emami et al. [57].

order partial differential equation that was solved numerically via finite element method. Fig. 22 shows an example of an air–water interface formed over a superhydrophobic surface comprised of randomly distributed posts with diameters ranging between 8 to 12 μm, and heights ranging between 50 to 51 μm, leading to a gas fraction of 65%. The deflection of the interface under a hydrostatic pressure of 3400 Pa can be seen. The posts are assumed to be made of a material with a contact angle of 120°.

To study the stability of the air–water interface formed over superhydrophobic coatings composed of randomly oriented nanofibers, Bucher et al. [58] conducted a series of FM simulations in 3-D virtual domains resembling the internal microstructure of electrospun fiber mats.

Fig. 23 shows an example of the FM simulations for two different hydrostatic pressures conducted by Bucher et al. The solid volume fraction and fiber diameter are 10% and 500 nm, respectively. It can be seen that, by increasing the pressure, the water (red color) fills a greater fraction of the pore space. Fig. 24 shows the critical pressure as a function of the coating's morphology for bimodal (composed of two different fiber diameters) fibrous media with random fiber orientations in terms of solid volume fraction and fine fiber diameter, d_f. It can be seen that critical pressure increases with increasing solid volume fraction or fine fiber diameter, when other microstructural parameters are held constant.
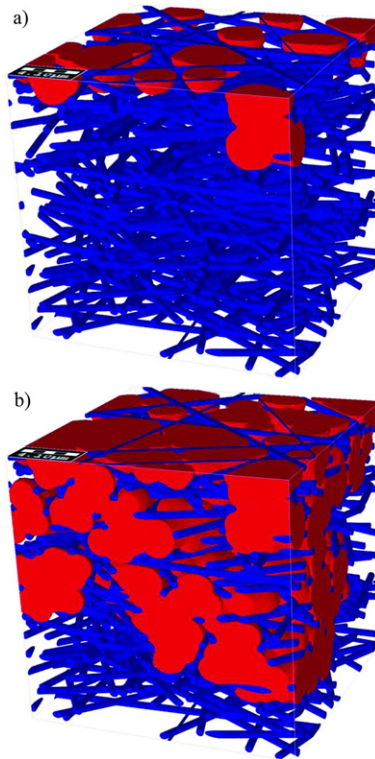
Fig. 23. A visualization of two stages of water intrusion into a unimodal fibrous structure with random in-plane fiber orientation, using the full-morphology method. Corresponding pressures are: (a) 58.983 kPa; (b) 77.333 kPa. The non-wetting fluid (water) represented in the red region is made up of spheres fitted into the domain. Figure adapted from Bucher et al. [58].
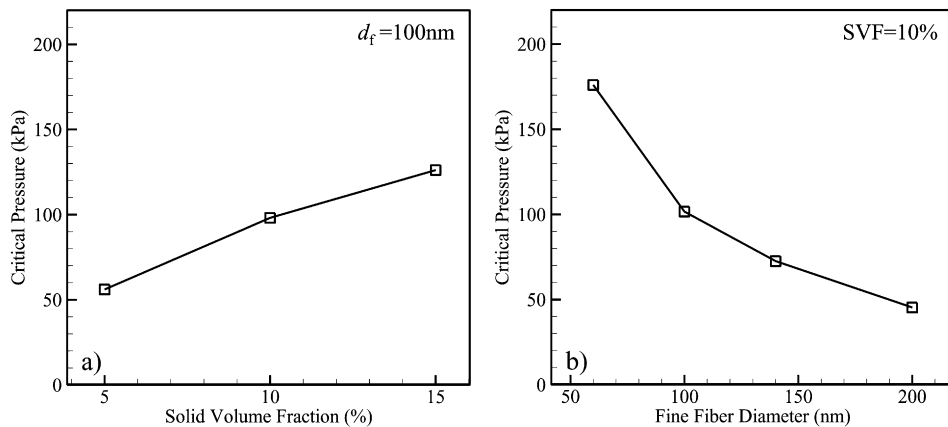

Fig. 24. Critical pressure predictions for layered, randomly oriented media compared against variations in one of four microstructural parameters: (a) solid volume fraction; (b) fiber diameter. For both (a) and (b), coarse-to-fine fiber diameter ratio (R_{cf}) = 5 and coarse number fraction (n_c) = 0.1. Figure adapted from Bucher et al. [58].

5. Longevity characterization of superhydrophobic coatings

Even when the air–water interface on a superhydrophobic surface is mechanically stable, the surface is likely to lose its entrapped air content over time. This is especially the case when the surface is submerged. This effect is believed to be due to the dissolution of air in water, and is expected to accelerate when the hydrostatic pressure is increased, as the solubility of air in water increases with pressure.

Bobji et al. [59] used an optical technique to measure how long superhydrophobic surfaces can entrap air underwater (surface longevity) by measuring the number of shiny spots that indicate an interface between air and water. Similar studies were performed using a laser beam to investigate the effect of the surface structure on the longevity [60]. Moreover, Poetes et al. [61] used a similar technique for the same test, but for different superhydrophobic coatings. Samaha et al. [18]
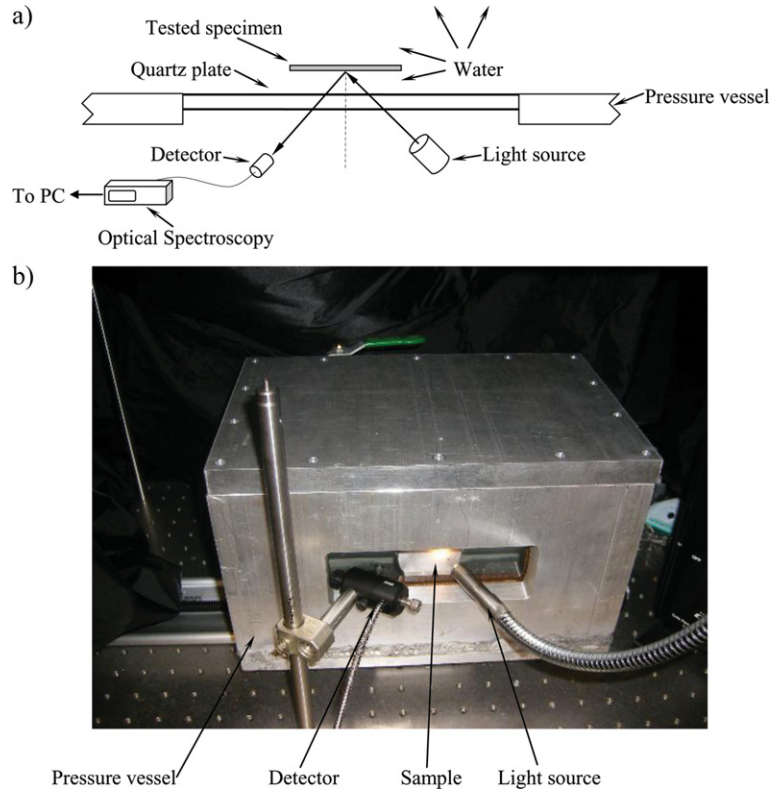
Fig. 25. (a) Schematic of the optical spectroscopy system. (b) Photograph of the pressure vessel. From Samaha et al. [18].

developed an optical technique to measure the longevity of submerged superhydrophobic coatings subjected to different environmental conditions. They used an optical spectroscopy system to quantify the intensity of reflected light in the visible range scattered from the surface (Fig. 25). The time-dependent light reflection intensity was measured at both a single wavelength and integrated over a range of wavelengths. Note that it is important to be able to measure the hydrophobicity of a surface *in situ* because the traditional contact angle or rheometer measurements may not necessarily represent the environment in which a surface may operate in practice. This includes, but is not limited to a broad range of time-dependent hydrostatic pressures (i.e. depths), and different degrees of salinity and/or air saturation. It is also of particular importance to be able to test a surface hydrophobicity over time under moving or still water. The optical spectroscopy system proposed by Samaha et al. can be utilized as a noninvasive method to measure surface hydrophobicity under the above conditions.

Fig. 26 shows the normalized reflected light intensity as a function of time and wavelength for an electrospun fibrous coating (discussed in Section 3.2) submerged in water for 166.5 h. The light intensity decreases with time at all wavelengths, which indicates a reduction in the volume of the entrapped air over time, and so the superhydrophobicity of the surface. Fig. 27 shows the normalized average reflected light intensity (the integral of the light intensity over all wavelengths divided by the wavelength range). The results shown in this figure were obtained under atmospheric pressure. It can be seen from Fig. 27 that the average reflected light intensity decreased by about 27% after 166.5 h of continuous submersion in water.

For validation, Samaha et al. [18] compared the results obtained from the optical system with drag-reduction data using the rheometer discussed in Section 3.2. Fig. 28 shows the measured drag reduction versus strain rate for the fibrous coating before and after immersing the coated sample in water. The results indicate that the coating is still capable of reducing the drag after 166.5 hours of immersion in water under atmospheric pressure. The average drag reduction was decreased by about 31% with respect to that of the fresh specimen, which is close to that reduction in light intensity using the optical system.

For further validation static contact angles and contact-angle hysteresis are measured for the same sample using a ramé-hart goniometer (model number 100-25-A). The measurements indicate that the results of the light-scattering surface characterization technique correlate strongly with both contact-angle and drag-reduction measurements. The contact-angle hysteresis measurements further validate the light-scattering method. Low-contact-angle hysteresis was observed for the fresh superhydrophobic sample. However, more noticeable hysteresis was seen for aged specimens. These results are consistent with the observations of other researchers [21,62–64]. *In situ* characterization of submerged hydrophobic surfaces using optical light scattering represents a new and useful tool for real-time estimation of hydrophobicity and drag reduction.
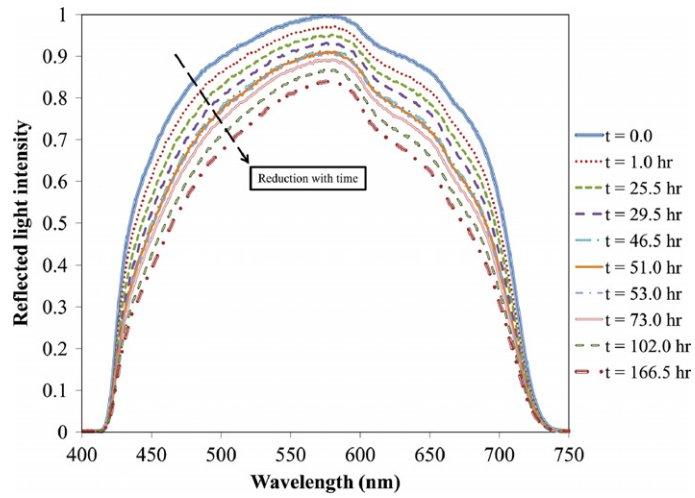
Fig. 26. Reduction in reflected light intensity with time for a spun-fiber sample. Measurements are taken for the entire visible-light spectrum. From Samaha et al. [18].
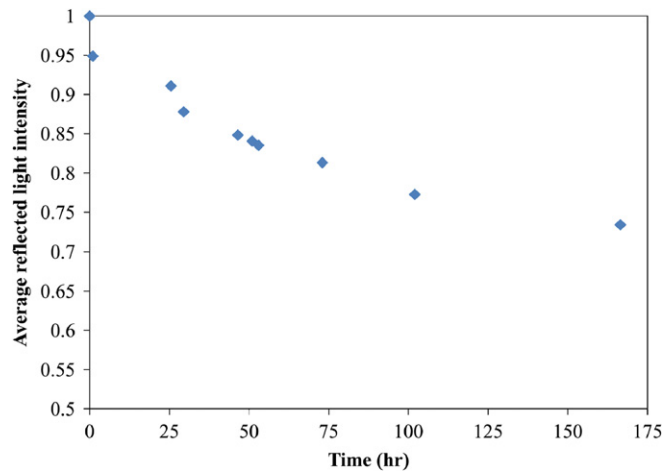

Fig. 27. Average reflected light intensity reduction with time for a spun-fiber sample. From Samaha et al. [18].
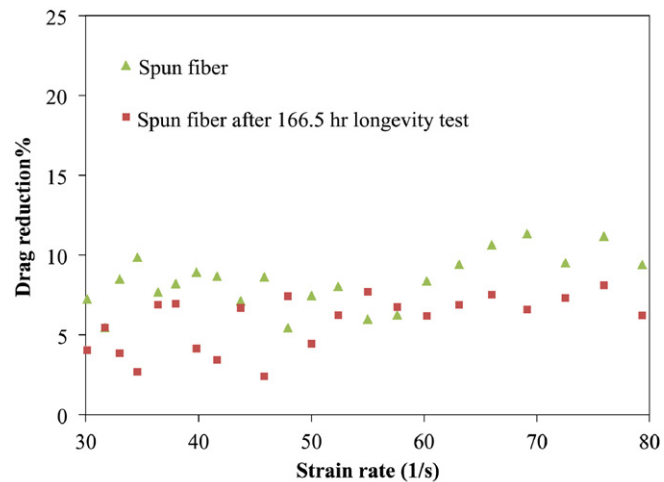

Fig. 28. Drag reduction versus strain rate. From Samaha et al. [18].

6. Future outlook

Superhydrophobic surfaces were demonstrated by several experimental, numerical, and analytical studies to reduce drag for both laminar and turbulent flows. This reinforces the optimistic view that these surfaces could be used for drag-reduction purposes, especially in marine environments. For example, it is well known that submarines consume a large amount of fuel to overcome the skin-friction drag produced on their bodies. Intensive flow-control studies have been performed to develop different active, reactive, and passive methods to reduce this drag force. Superhydrophobic coatings are aimed to be utilized as a passive method and may potentially become a viable alternative to the more complex and energy consuming active or reactive flow-control techniques such as wall suction/blowing. However, there are still significant issues that need to be resolved in order for the manufacturing of such coatings to be feasible. First of all, the microstructure of the coating should be strong enough to sustain the developed shear stress without erosion especially for turbulent flow. Secondly, the coating should keep its hydrophobicity for an acceptable time frame (reasonable longevity). Moreover, if the coating becomes hydrophilic, an infield method should be developed to rejuvenate the surface to return it to its hydrophobic state. Third, the coating should be durable enough to sustain environmental conditions such as water salinity, depth, circulation, and biofouling. Finally, the fabrication processes should be extended from lab scale to large industrial scale applications. All of these issues require further research and development before superhydrophobic coatings could be utilized under realistic circumstances.

7. Conclusions

Currently, the lotus effect is employed to produce water-repellent paint and fabrics for self-cleaning or waterproofing applications. However, it also could be utilized for mobile submerged surfaces to generate drag reduction and slip flow, which takes place at the interface between the entrapped air and water. The performance of the surface is characterized by slip length, which is strongly affected by gas fraction, both for both laminar and turbulent flow.

For submerged superhydrophobic surfaces, this interface is stable against the transition from non-wetted (Cassie) state to wetted (Wenzel) state due to pressure. Several theoretical analyses and numerical simulations have been performed to estimate the critical pressure for different microstructures. The longevity of these surfaces can be measured via drag-reduction data using a rheometer or contact-angle measurements. Noninvasive optical measuring system can measure the real-time effects of such environments.

Microfabrication could be utilized to produce superhydrophobic surfaces with different properties. However, it cannot be applied to large-scale bodies with arbitrary shape. Simpler lower-cost fabrication techniques are being developed to meet those requirements. Experimental measurements and numerical simulations have been performed to characterize the hydrophobicity and longevity of these surfaces in comparison with those produced via ordered-microstructure processes. Both techniques are under research and development to produce the optimum surface that can produce high drag reduction and possesses reasonable longevity. Such coatings will ultimately be used on submarines, torpedoes, and naval ships for the purpose of reducing skin-friction drag in both the laminar and turbulent boundary layers surrounding these vessels when cruising in seawater.

Acknowledgements

References

[1] C. Neinhuis, W. Barthlott, Characterization and distribution of water-repellent, self-cleaning plant surfaces, Ann. Bot. 79 (1997) 667–677.
[2] X. Gao, L. Jiang, Water-repellent legs of water striders, Nature 432 (2004) 36.
[3] J.P. Rothstein, Slip on superhydrophobic surfaces, Annu. Rev. Fluid Mech. 42 (2010) 89–109.
[4] C. Lee, C.-J. Kim, Maximizing the giant slip on superhydrophobic microstructures by nanostructuring their sidewalls, Langmuir 25 (2009) 12812–12818.
[5] B. Emami, T.M. Bucher, H.V. Tafreshi, D. Pestov, M. Gad-el-Hak, G.C. Tepper, Simulation of meniscus stability in superhydrophobic granular surfaces under hydrostatic pressures, Colloids Surf. A 385 (2011) 95–103.
[6] H. Yang, Y. Deng, Preparation and physical properties of superhydrophobic papers, J. Colloid Interface Sci. 325 (2008) 588–593.
[7] S.D. Bhagat, Y.-H. Kim, K.-H. Suh, Y.-S. Ahn, J.-G. Yeo, J.-H. Han, Super hydrophobic silica aerogel powders with simultaneous surface modification, solvent exchange and sodium ion removal from hydrogels, Microporous Mesoporous Mater. 112 (2008) 504–509.
[8] M. Ma, Y. Mao, M. Gupta, K.K. Gleason, G.C. Rutledge, Superhydrophobic fabrics produced by electrospinning and chemical vapor deposition, Macromolecules 38 (2005) 9742–9748.
[9] A. Singh, L. Steely, H.R. Allcock, Poly[bis(2,2,2-trifluoroethoxy)phosphazene] superhydrophobic nanofibers, Langmuir 21 (2005) 11604–11607.
[10] M. Zhu, W. Zuo, H. Yu, W. Yang, Y. Chen, Superhydrophobic surface directly created by electrospinning based on hydrophilic material, J. Mater. Sci. 41 (2006) 3793–3797.
[11] F.O. Ochanda, M.A. Samaha, H.V. Tafreshi, G.C. Tepper, M. Gad-el-Hak, Fabrication of superhydrophobic fiber coatings by DC-biased AC-electrospinning, J. Appl. Polym. Sci. 123 (2012) 1112–1119.
[12] Y.T. Cheng, D.E. Rodak, C.A. Hayden, Effects of micro- and nano-structures on the self-cleaning behavior of lotus leaves, Nanotechnology 17 (2006) 1359–1362.

[13] K. Koch, B. Bhushan, Y.C. Jung, W. Barthlott, Fabrication of artificial Lotus leaves and significance of hierarchical structure for superhydrophobicity and low adhesion, Soft Matter 5 (2009) 1386–1393.
[14] http://www.flickr.com/photos/rachelyin/3203932476/.
[15] http://www.hk-phy.org/atomic_world/lotus/lotus01_e.html.
[16] http://www.thenakedscientists.com/HTML/articles/article/biomimeticsborrowingfrombiology/.
[17] M. Gad-el-Hak, Flow Control: Passive, Active, and Reactive Flow Management, Cambridge University Press, London, United Kingdom, 2000.
[18] M.A. Samaha, F.O. Ochanda, H.V. Tafreshi, G.C. Tepper, M. Gad-el-Hak, *In situ*, non-invasive characterization of superhydrophobic coatings, Rev. Sci. Instrum. 82 (2011) 045109.
[19] M. Gad-el-Hak, The fluid mechanics of microdevices – The Freeman scholar lecture, J. Fluids Eng. 121 (1999) 5–33.
[20] E. Lauga, M.P. Brenner, H.A. Stone, Microfluidics: the no-slip boundary condition, in: C. Tropea, A. Yarin, J. Foss (Eds.), Handbook of Experimental Fluid Dynamics, Springer, New York, 2007.
[21] J. Bico, C. Marzolin, D. Quéré, Pearl drops, Europhys. Lett. 47 (1999) 220–226.
[22] M. Callies, Y. Chen, F. Marty, A. Pépin, D. Quéré, Microfabricated textured surfaces for super-hydrophobicity investigations, Microelectron. Eng. 78–79 (2005) 100–105.
[23] C. Lee, C.-H. Choi, C.-J. Kim, Structured surfaces for giant liquid slip, Phys. Rev. Lett. 101 (2008) 064501.
[24] C.L.M.H. Navier, Memoire sur les lois du mouvement des fluides, Mem. Acad. R. Sci. Inst. France 6 (1823) 389–440.
[25] E. Lauga, H.A. Stone, Effective slip in pressure-driven Stokes flow, J. Fluid Mech. 489 (2003) 55–77.
[26] J. Ou, J.B. Perot, J.P. Rothstein, Laminar drag reduction in microchannels using ultrahydrophobic surfaces, Phys. Fluids 16 (2004) 4635–4643.
[27] J. Ou, J.P. Rothstein, Direct velocity measurements of the flow past drag-reducing ultrahydrophobic surfaces, Phys. Fluids 17 (2005) 103606.
[28] J. Davies, D. Maynes, B.W. Webb, B. Woolford, Laminar flow in a microchannel with superhydrophobic walls exhibiting transverse ribs, Phys. Fluids 18 (2006) 087110.
[29] D. Maynes, K. Jeffs, B. Woolford, B.W. Webb, Laminar flow in a microchannel with hydrophobic surface patterned microribs oriented parallel to the flow direction, Phys. Fluids 19 (2007) 093603.
[30] C. Ybert, C. Barentin, C.-B. Cécile, P. Joseph, L. Bocquet, Achieving large slip with superhydrophobic surfaces: Scaling laws for generic geometries, Phys. Fluids 19 (2007) 123601.
[31] Y.P. Cheng, C.J. Teo, B.C. Khoo, Microchannel flow with superhydrophobic surfaces: Effects of Reynolds number and pattern width to channel height ratio, Phys. Fluids 21 (2009) 122004.
[32] R. Daniello, N.E. Waterhouse, J.P. Rothstein, Turbulent drag reduction using superhydrophobic surfaces, Phys. Fluids 21 (2009) 085103.
[33] M. Martell, J.B. Perot, J.P. Rothstein, Direct numerical simulations of turbulent flows over superhydrophobic surfaces, J. Fluid Mech. 620 (2009) 31–41.
[34] A.M.J. Davis, E. Lauga, The friction of a mesh-like super-hydrophobic surface, Phys. Fluids 21 (2009) 113101.
[35] B. Woolford, J. Prince, D. Maynes, B.W. Webb, Particle image velocimetry characterization of turbulent channel flow with rib patterned superhydrophobic walls, Phys. Fluids 21 (2009) 085106.
[36] M.A. Samaha, H.V. Tafreshi, M. Gad-el-Hak, Modeling drag reduction and meniscus stability of superhydrophobic surfaces comprised of random roughness, Phys. Fluids 23 (2011) 012001.
[37] D. Huang, C. Sendner, D. Horinek, R. Netz, L. Bocquet, Water slippage versus contact angle: a quasiuniversal relationship, Phys. Rev. Lett. 101 (2008) 226101.
[38] C. Sendner, D. Horinek, L. Bocquet, R. Netz, Interfacial water at hydrophobic and hydrophilic surfaces: slip, viscosity, and diffusion, Langmuir 25 (2009) 10768–10781.
[39] L. Bocquet, E. Charlaix, Nanofluidics, from bulk to interfaces, Chem. Soc. Rev. 39 (2010) 1073–1095.
[40] J. Bico, U. Thiele, D. Quéré, Wetting of textured surfaces, Colloids Surf. A 206 (2002) 41–46.
[41] C. Henoch, T.N. Krupenkin, P. Kolodner, J.A. Taylor, M.S. Hodes, A.M. Lyons, C. Peguero, K. Breuer, Turbulent drag reduction using superhydrophobic surfaces, in: 3rd AIAA Flow Control Conference, San Francisco, California, 2006, p. 3192.
[42] C.-H. Choi, C.-J. Kim, Large slip of aqueous liquid flow over a nanoengineered superhydrophobic surface, Phys. Rev. Lett. 96 (2006) 066001.
[43] S. Sarkar, S. Deevi, G. Tepper, Biased AC electrospinning of aligned polymer nanofibers, Macromol. Rapid Commun. 28 (2007) 1034–1039.
[44] http://commons.wikimedia.org/wiki/File:Water-strider-1.jpg.
[45] X.-Q. Feng, X. Gao, Z. Wu, L. Jiang, Q.-S. Zheng, Superior water repellency of water strider legs with hierarchical structures: experiments and analysis, Langmuir 23 (2007) 4892–4896.
[46] J.W.M. Bush, D.L. Hu, Walking on water: biolocomotion at the interface, Annu. Rev. Fluid Mech. 38 (2006) 339–369.
[47] D.L. Hu, B. Chan, J.W.M. Bush, The hydrodynamics of water strider locomotion, Nature 424 (2003) 663–666.
[48] D.L. Hu, M. Prakash, B. Chan, J.W.M. Bush, Water-walking devices, Exp. Fluids 43 (2007) 769–778.
[49] G.M. Stonedahl, J.D. Lattin, The Gerridae or water striders of Oregon and Washington (Hemiptera:Heteroptera), Technical Bulletin 144, Oregon State University, 1982, pp. 1–36.
[50] M.R. Flynn, J.W.M. Bush, Underwater breathing: the mechanics of plastron respiration, J. Fluid Mech. 608 (2008) 275–296.
[51] N.A. Patankar, Transition between superhydrophobic states on rough surfaces, Langmuir 20 (2004) 7097–7102.
[52] L. Barbieri, E. Wagner, P. Hoffmann, Water wetting transition parameters of perfluorinated substrates with periodically distributed flat-top microscale obstacles, Langmuir 23 (2007) 1723–1734.
[53] C.W. Extrand, Criteria for ultralyophobic surfaces, Langmuir 20 (2004) 5013–5018.
[54] C.W. Extrand, Designing for optimum liquid repellency, Langmuir 22 (2006) 1711–1714.
[55] Q.S. Zheng, Y. Yu, Z.H. Zhao, Effects of hydraulic pressure on the stability and transition of wetting modes of superhydrophobic surfaces, Langmuir 21 (2005) 12207–12212.
[56] A. Okabe, B. Boots, K. Sugihara, S.N. Chiu, D.G. Kendall, Spatial Tessellations: Concepts and Applications of Voronoi Diagrams, second edition, John Wiley & Sons Ltd., Chichester, UK, 2000.
[57] B. Emami, H.V. Tafreshi, M. Gad-el-Hak, G.C. Tepper, Predicting shape and stability of air–water interface on superhydrophobic surfaces with randomly distributed, dissimilar posts, Appl. Phys. Lett. 98 (2011) 203106.
[58] T.M. Bucher, B. Emami, H.V. Tafreshi, M. Gad-el-Hak, G.C. Tepper, Modeling resistance of nanofibrous superhydrophobic coatings to hydrostatic pressures: the role of microstructure, Phys. Fluids, submitted for publication.
[59] M. Bobji, S.V. Kumar, A. Asthana, R.N. Govardhan, Underwater sustainability of the "Cassie" state of wetting, Langmuir 25 (2009) 12120–12126.
[60] M. Sakai, T. Yanagisawa, A. Nakajima, Y. Kameshima, K. Okada, Effect of surface structure on the sustainability of an air layer on superhydrophobic coatings in a water–ethanol mixture, Langmuir 25 (2009) 13–16.
[61] R. Poetes, K. Holtzmann, K. Franze, U. Steiner, Metastable underwater superhydrophobicity, Phys. Rev. Lett. 105 (2010) 166104.
[62] D. Quéré, A. Lafuma, J. Bico, Slippy and sticky microtextured solids, Nanotechnology 14 (2003) 1109–1112.
[63] A. Lafuma, D. Quéré, Superhydrophobic states, Nat. Mater. 2 (2003) 457–460.
[64] D. Quéré, Wetting and roughness, Annu. Rev. Mater. Res. 38 (2008) 71–99.